CRYSTAL GROWTH & DESIGN

pubs.acs.org/crystal

Article

Crystal Growth and Elemental Homogeneity of the Multicomponent Rare-Earth Garnet $(Lu_{1/6}Y_{1/6}Ho_{1/6}Dy_{1/6}Tb_{1/6}Gd_{1/6})_3Al_5O_{12}$

Matheus Pianassola,* Madeline Loveday, Bryan C. Chakoumakos, Merry Koschan, Charles L. Melcher, and Mariya Zhuravleva

Cite This: *Cryst. Growth Des.* 2020, 20, 6769–6776

Read Online

ACCESS | Metrics & More | Article Recommendations | Supporting Information

ABSTRACT: High-entropy aluminum garnets were grown as bulk single crystals using the micro-pulling-down method, taking the synthesis of complex ceramics a step further from the conventional preparation of polycrystalline materials. We studied the effects of growth parameters on the elemental distribution in high optical quality crystals of $(Lu_{1/6}Y_{1/6}Ho_{1/6}Dy_{1/6}Tb_{1/6}Gd_{1/6})_3Al_5O_{12}$ containing six cations (yttrium and rare-earths) taken in equimolar amounts. A single garnet structure was confirmed by powder X-ray diffraction. Electron microprobe measurements were obtained to correlate the radial distribution of rare-earth elements with pulling rates and molten zone height. The nature of the elemental distribution in the radial direction was associated with ionic radius: smaller rare-earths concentrated in the center of the crystal, while larger rare-earths segregated toward the outer edge of the cylindrical crystal. Faster pulling rates led to a flattening of the concentration profiles toward the nominal concentration, promoting a more homogeneous radial elemental distribution, while varying the molten zone height did not have a significant effect. The demonstrated success with crystal growth enables the practical availability of single crystals of multicomponent aluminum garnets for further discovery of new phenomena and applications.

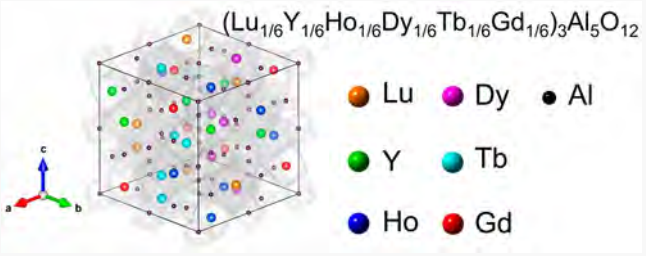

1. INTRODUCTION

Commercial rare-earth aluminum garnet (REAG) crystals usually have one or two types of rare-earths (REs); however, recent studies on high-entropy ceramics suggest that mixing five or more elements in equimolar amounts may enhance functional properties.[1] REAG crystals are widely used and investigated for luminescent applications. Typical compositions include $Y_3Al_5O_{12}$:Nd and $Lu_3Al_5O_{12}$:Pr used as a lasing medium and a scintillator, respectively.[2,3] The general formula of an REAG is $RE_3Al_5O_{12}$, where RE is a rare-earth element. In the cubic garnet structure, the RE occupies a dodecahedral crystallographic site, while Al occupies tetrahedral and octahedral sites. Because of the geometry of the dodecahedral site, only REs smaller than Gd^{3+} can form an aluminum garnet without disrupting the Al−O framework.[4] Small amounts of larger cations such as Nd^{3+} and Pr^{3+} can be added into REAG as dopants without major lattice distortions. The functional performance of REAG crystals is commonly explored by admixing two or three elements in the RE or Al sites.[5−10] Although the interesting compositional design of high-entropy oxides has been applied to many compounds,[1] high-entropy REAG single crystals with multiple principal REs have not yet been reported. High-entropy oxides are single-phase materials that contain five or more principal cations and have a configurational entropy ΔS_{conf} higher than $1.5R$ (where R is the universal gas constant). ΔS_{conf} is maximized by having equimolar amounts of cations, which then minimizes the Gibbs free anergy of mixing, favoring the thermodynamic stabilization of a single phase with multiple cations.[11]

Following the general trend of high-entropy metallic alloys,[11] the possibility of obtaining exceptional functional properties has inspired the investigation of high-entropy oxides.[1,12] A few RE-based high-entropy polycrystalline ceramics have been reported including sesquioxide,[13,14] silicate,[15,16] zirconate,[17] phosphate,[18] aluminum perovskite,[19] and aluminum garnet[20] structures. In previous reports, the availability of high-entropy oxides was restricted to the synthesis methods for ceramics or thin films.[21] To consider highly complex REAG compositions as prospective host materials for applications such as lasing and scintillation, high optical quality single crystals need to be synthesized to enable the characterization of luminescence properties such as optical transmittance and light yield. To the best of our knowledge, bulk single-crystal high-entropy oxide materials have not yet been synthesized.

Received: June 27, 2020
Revised: September 1, 2020
Published: September 2, 2020

https://dx.doi.org/10.1021/acs.cgd.0c00887
Cryst. Growth Des. 2020, 20, 6769–6776

In this work, the crystal growth of high optical quality high-entropy aluminum garnet $(Lu_{1/6}Y_{1/6}Ho_{1/6}Dy_{1/6}Tb_{1/6}Gd_{1/6})_3Al_5O_{12}$ was demonstrated, and distribution of the six REs was investigated. For simplicity we refer to yttrium as one of the REs in this multicomponent garnet. These six REs were selected for this study due to their wide range of RE^{3+} ionic radii, 0.097−1.06 Å.[22] Most studies into the elemental homogeneity of micro-pulling-down crystals focus on the distribution of small dopant concentrations[23−26] or solid solutions with a smaller number of constituents.[27] Here we used electron microprobe analysis to investigate the distribution of the six principal REs in a highly complex aluminum garnet crystal.

Single-crystal growth of the one-component garnets formed by each of these six RE and their structural stability have been reported. While $Lu_3Al_5O_{12}$, $Y_3Al_5O_{12}$, $Ho_3Al_5O_{12}$, and $Dy_3Al_5O_{12}$ single crystals can be produced from the melt with relative ease,[3,28−30] the crystal growth of $Gd_3Al_5O_{12}$ or $Tb_3Al_5O_{12}$ is a challenge, since both compounds melt incongruently.[4,31−34] Despite this challenge, we grew $(Lu_{1/6}Y_{1/6}Ho_{1/6}Dy_{1/6}Tb_{1/6}Gd_{1/6})_3Al_5O_{12}$ crystals from a stoichiometric melt. This success expands the compositional space of REAG toward areas with higher configurational entropy and enables the practical availability of single crystals for the investigation of fundamental and functional properties. Although the crystals studied in this work satisfy the definition of a high entropy oxide,[1] here we refrain from referring to them as entropy-stabilized materials, since the precise mechanism of phase stabilization is still unknown.

2. EXPERIMENTAL SECTION

2.1. Starting Materials. In preparation for the crystal-growth experiments, the following powder materials were dried at 800 °C for 5 h in air: Lu_2O_3 (Yarmouth Materials, 99.999%), Y_2O_3 (Yarmouth Materials, 99.999%), Ho_2O_3 (Alfa Aesar, 99.99%), Dy_2O_3 (Alfa Aesar, 99.99%), Tb_4O_7 (Alfa Aesar, 99.9%), Gd_2O_3 (American Elements, 99.999%), and Al_2O_3 (Yarmouth Materials, 99.99%). One-gram stoichiometric mixtures of the dried powders were mixed by manual agitation in 4 mL glass vials.

2.2. Crystal Growth. Five cylindrical single crystals were grown using a KDN Dai-Ichi Kiden micro-pulling-down furnace equipped with an RF generator model TR-02001 operated at 26 kVA. A schematic representation of the furnace setup is shown in Figure 1, which is similar to previously reported work.[35] A ⌀16 mm iridium crucible with a ⌀3 mm die and a ⌀0.5 mm capillary channel was used as a melt reservoir. Growth was initiated by touching the outlet of the capillary channel with a Czochralski-grown $Lu_3Al_5O_{12}$ crystal seed. Crystal growth proceeds by continuous lowering of the seed, which leads to a controlled solidification of the melt. An appropriate temperature gradient is maintained by use of an Ir after-heater immediately below the crucible. An appropriate temperature gradient is judged by the visual observation of the stable shape and height of the molten zone. The melt is supplied to the molten zone through the crucible capillary.

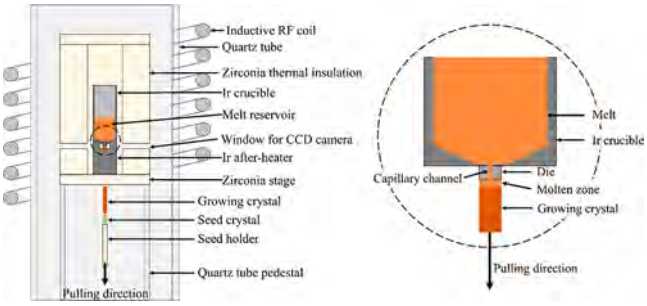

Figure 1. Schematic representation of the micro-pulling-down crystal growth setup (left). The circled region is shown on the right with detail; the after-heater is omitted for simplicity.

A charge-coupled device (CCD) camera was focused on the bottom of the crucible die to allow real-time visualization of seeding and monitoring of the molten zone. The shape and height of the molten zone affect the shape of the crystal, its structural quality, the mass exchange in the molten zone, and, consequently, the spatial distribution of the elements in the grown crystal.[35] Oxidation of the crucible and the deposition of possible volatiles on the lower portion of the outer quartz tube were prevented by use of a growth atmosphere composed of flowing nitrogen. The RF generator power was ramped over a period of 2 h to achieve the melting point, which was visually determined by probing the capillary with the seed and observing the presence of molten material.

Five crystals were grown with differing molten zone heights and pulling rates, chosen to study the effect of these parameters on the elemental distribution both radially and axially throughout the crystal. Crystal growth was initiated ∼10 min after melting with an initial pulling rate of 0.05 mm/min. One crystal was grown with a molten zone height of ∼100 μm and pulling rate of 0.05 mm/min throughout the entire growth process. Four crystals were grown with a molten zone height of ∼300 μm; after these crystals reached the full 3 mm diameter, the pulling rate was either kept at 0.05 mm/min or gradually increased. For the crystal pulled at 0.10 mm/min, the target pulling rate was achieved at 1.8 mm from the seed end; similarly, the crystals pulled at 0.15 and 0.20 mm/min reached the target pulling rate at 2.4 and 3.2 mm from the seed end, respectively. The fluctuation of the molten zone height was visually estimated to be in the range of 25−50 μm. The melt temperature is directly proportional to the visible molten zone height, which was controlled by manually adjusting the RF generator power. A stable molten zone is essential for growth stability and crystal diameter control. After the growth was finished, the RF generator power ramp-down was conducted over a period of 4 h. A small amount of material remained at the bottom of the crucible after all growth experiments. A list of crystals studied and their respective pulling rates and molten zone heights is in Table 1.

Table 1. A List of Crystals Grown with Respective Pulling Rates and Molten Zone Depths[a]

crystal	pulling rate (mm/min)	molten zone height (μm)
005−100	0.05	∼100
005−300	0.05	∼300
010−300	0.10	∼300
015−300	0.15	∼300
020−300	0.20	∼300

[a]The naming convention used is "pulling rate−molten zone height".

2.3. Density Measurements. The crystal density was measured by the Archimedes principle method using a Sartorius YDK 01 Density Determination Kit with a Sartorius CP324 S balance. Deionized water at room temperature was used as the immersion liquid.

2.4. Powder X-ray Diffraction. To identify the crystalline phase, each crystal was cut in half longitudinally, and one of the halves was ground in a mortar for room-temperature powder X-ray diffraction (XRD). Patterns were obtained with a Panalytical Empyrean diffractometer in the Bragg−Brentano geometry using a Cu Kα X-ray source at 45 kV and 40 mA. Phase analysis and lattice parameters were evaluated via Rietveld refinements with the General Structure Analysis System II software (GSASII). A goodness-of-fit value smaller than 1.60 was achieved for all refinements.

2.5. Single-Crystal X-ray Diffraction. Two crystal fragments (∼0.001 mm^3) were cut from the center and outer surface of the crystal 005−100. The fragments were suspended in the mineral oil of

https://dx.doi.org/10.1021/acs.cgd.0c00887
Cryst. Growth Des. 2020, 20, 6769−6776

a plastic loop attached to a copper pin/goniometer. Single-crystal diffraction data were collected at 260 K using a Rigaku XtaLAB PRO diffractometer with graphite monochromated Mo Kα radiation (λ = 0.710 73 Å, 50 kV, and 40 mA) equipped with a Rigaku HyPix-6000HE detector and an Oxford N-HeliX cryocooler. Peak indexing and integration were done using the Rigaku Oxford Diffraction CrysAlisPro software.[36] An empirical absorption correction was applied using the SCALE3 ABSPACK algorithm as implemented CrysAlisPro. The SHELXL-2013 and WinGX software packages were used for data processing and structure refinement.[37,38] The structure refinements were made with oxygen atom positional coordinates, anisotropic atomic displacement parameters, an extinction parameter, and the scale factor.

2.6. Electron Microprobe Analysis. A longitudinal half of each crystal was embedded in epoxy for the elemental composition analysis of crystal cross sections by electron probe microanalysis (EPMA) with a CAMECA SX100 Electron Microprobe. The instrument is equipped with high-speed backscattered electron (BSE) detectors and four wavelength-dispersive spectrometers (WDS). Images were obtained by detecting the backscattered electrons, and compositional information was acquired by detecting characteristic X-rays by WDS. The instrumental voltage and current were 15 kV and 30 nA, respectively. The probe point size was 1 μm, and the excitation area diameter was in the 2−3 μm range. Radial distribution profiles were obtained by collecting data at 100 μm steps; multiple profiles were spaced 2.5 mm apart.

3. RESULTS AND DISCUSSION

3.1. Grown Crystals. All five 3 mm diameter crystals grown are yellow and crack-free, except the crystal pulled at 0.20 mm/min, which has a small crack close to the seed end as indicated in Figure 2 by a white dashed oval. The formation of this crack was visually observed in real time and started propagating when the crystal was still being pulled at 0.05 mm/min; therefore, the crack formation is not correlated with the faster pulling rate. The different pulling rates and molten zone heights used did not affect the visually observable quality of the crystals. Images of the molten zone of crystals 005−100 and 005−300 are shown in the Supporting Information in Figure S1 for comparison of the monitored molten zone height. The crystal density measured by the Archimedes method is 5.95 g/cm^3.

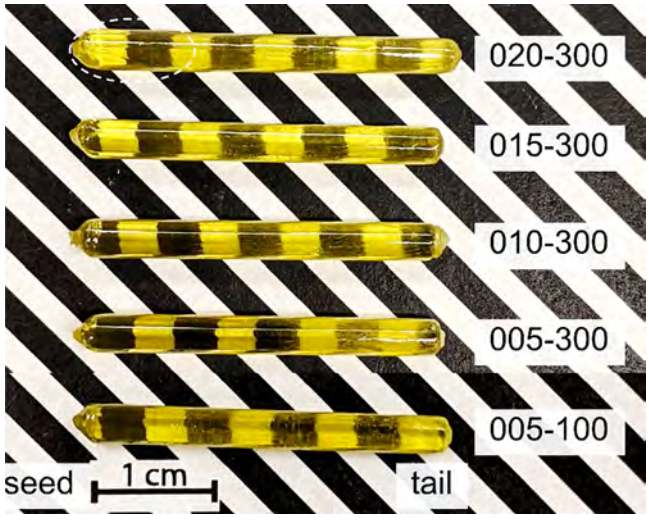

Figure 2. Single crystals of $(Lu_{1/6}Y_{1/6}Ho_{1/6}Dy_{1/6}Tb_{1/6}Gd_{1/6})_3Al_5O_{12}$ were grown with varying growth parameters, see Table 1. All crystals are cylinders with 3 mm in diameter. A white dashed oval indicates the area with a crack in the crystal pulled at 0.20 mm/min.

3.2. Crystal Structure. *3.2.1. Powder XRD.* The $(Lu_{1/6}Y_{1/6}Ho_{1/6}Dy_{1/6}Tb_{1/6}Gd_{1/6})_3Al_5O_{12}$ crystals have a single garnet phase, as confirmed by the powder XRD patterns in Figure 3; reference YAG reflection peaks[39] are also plotted for comparison.

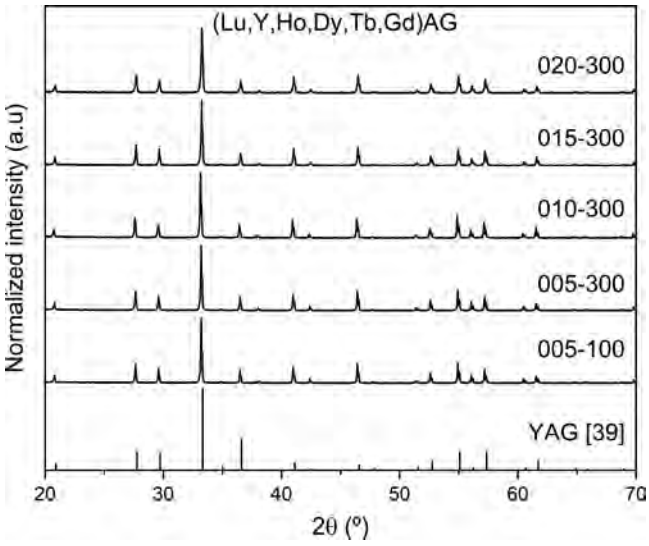

Figure 3. XRD patterns of $(Lu_{1/6}Y_{1/6}Ho_{1/6}Dy_{1/6}Tb_{1/6}Gd_{1/6})_3Al_5O_{12}$ powdered single crystals indicate a single garnet phase. YAG reflection peaks are plotted for comparison.[39]

height. Assuming a homogeneous mixture of the six REs throughout the whole crystal, one would expect the lattice parameter of the multicomponent composition to be close to the average taken from the lattice parameters of the corresponding one-component REAG, namely, LuAG,[40] YAG,[40] HoAG,[29] DyAG,[41] TbAG,[42] and GdAG.[40] Figure 4 includes the literature values of the lattice parameters of single-REAG as a function of rare-earth ionic radius for the 3+ oxidation state and coordination number VIII[22] (black circles). The lattice parameter of $(Lu_{1/6}Y_{1/6}Ho_{1/6}Dy_{1/6}Tb_{1/6}Gd_{1/6})_3Al_5O_{12}$ obtained from Rietveld refinement, 12.033(7) Å, is also plotted as a function of the calculated average ionic radius of the six REs, which is 1.023 Å (blue square). This lattice parameter is nearly identical to the calculated average value of the lattice parameters of the single-REAG, which is 12.025 Å. This indicates that the lattice parameter of a multicomponent garnet can be predicted based on the composition and ionic radius.

3.2.2. Single-Crystal XRD. The singe-crystal X-ray diffraction refinement parameters are given in the Supporting Information in Table S1. The number of elements on the RE site in $(Lu_{1/6}Y_{1/6}Ho_{1/6}Dy_{1/6}Tb_{1/6}Gd_{1/6})_3Al_5O_{12}$ makes site occupation refinements underdetermined, so the RE site occupation was held fixed at the nominal composition. The fractional atomic coordinates and equivalent isotropic displacement parameters are in Table S2. The oxygen coordinate is the same for both the center and edge samples of the boule, whereas the cell size is significantly different. The larger cell size for the edge sample implies that the RE elements with a smaller ionic radius are reduced somewhat relative to the larger REs, and the RE−O bond lengths are slightly longer, as would be expected, as seen in Table S1. The X-ray patterns showed

https://dx.doi.org/10.1021/acs.cgd.0c00887
Cryst. Growth Des. 2020, 20, 6769−6776

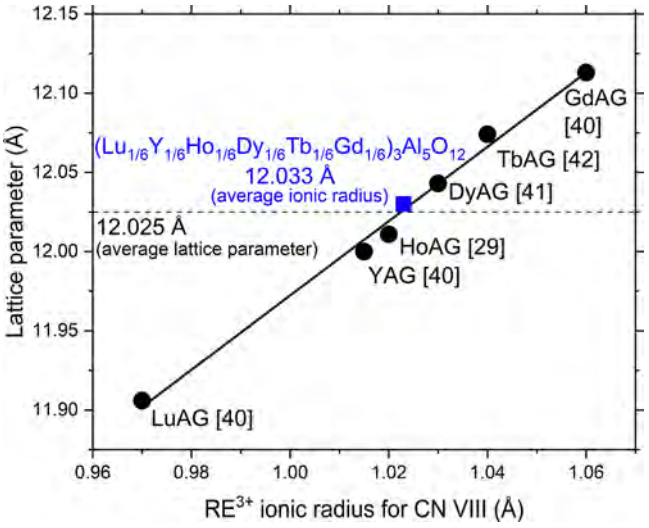

Figure 4. Literature values of the lattice parameters of single-REAG (referenced in the figure) as a function of rare-earth ionic radius for the 3+ oxidation state and coordination number VIII[22] (●). The experimentally obtained lattice parameter of $(Lu_{1/6}Y_{1/6}Ho_{1/6}Dy_{1/6}Tb_{1/6}Gd_{1/6})_3Al_5O_{12}$ (12.033 Å) is nearly identical to the calculated average value of the lattice parameters of the single-REAG (12.025 Å). The ionic radius of the RE ions in $(Lu_{1/6}Y_{1/6}Ho_{1/6}Dy_{1/6}Tb_{1/6}Gd_{1/6})_3Al_5O_{12}$ is plotted as the average of the six REs (■).

no obvious diffuse scattering, which suggests no short-range clustering of the REs.

3.3. Radial Distribution. *3.3.1. Relationship between Ionic Radii and the General Shape of Concentration Profiles.* EPMA results reveal a nonuniform radial elemental distribution, with some elements at a higher concentration in the center of the crystal, while other elements are at a higher concentration near the outer surface of the cylindrical crystal. As shown in Figure 4, the average ionic radius of the six REs in $(Lu_{1/6}Y_{1/6}Ho_{1/6}Dy_{1/6}Tb_{1/6}Gd_{1/6})_3Al_5O_{12}$ can be used to divide them into two groups: Group 1, which is comprised of the REs that are smaller than 1.023 Å, namely, Lu, Y, and Ho, and Group 2, which is comprised of the REs that are larger than that value, namely, Dy, Tb, and Gd. Figure S2 shows radial elemental profiles for the six REs measured at various distances from the seed end of the crystal 005−300. There is a clear correlation between the elemental distribution profiles and the RE ionic radius. On the one hand, the smaller elements of Group 1 concentrate in the center of the crystal and are preferentially incorporated into the crystal lattice as shown by their upwardly curved concentration profiles in Figure S2. On the other hand, the larger elements of Group 2 have downwardly curved profiles and therefore were rejected toward the outer surface of the crystal. Similar trends were observed for all crystals, which support the observation of a larger unit cell at the outer edge of the crystal in single-crystal XRD, as seen in Table S1. These results indicate that elements in Group 1 have segregation coefficients $k > 1$ and are readily incorporated into the crystal lattice, while elements of Group 2 have a $k < 1$ and are rejected from the growth interface. Considering the average RE ionic radius as the size of the hosting site for the RE elements, our observations are

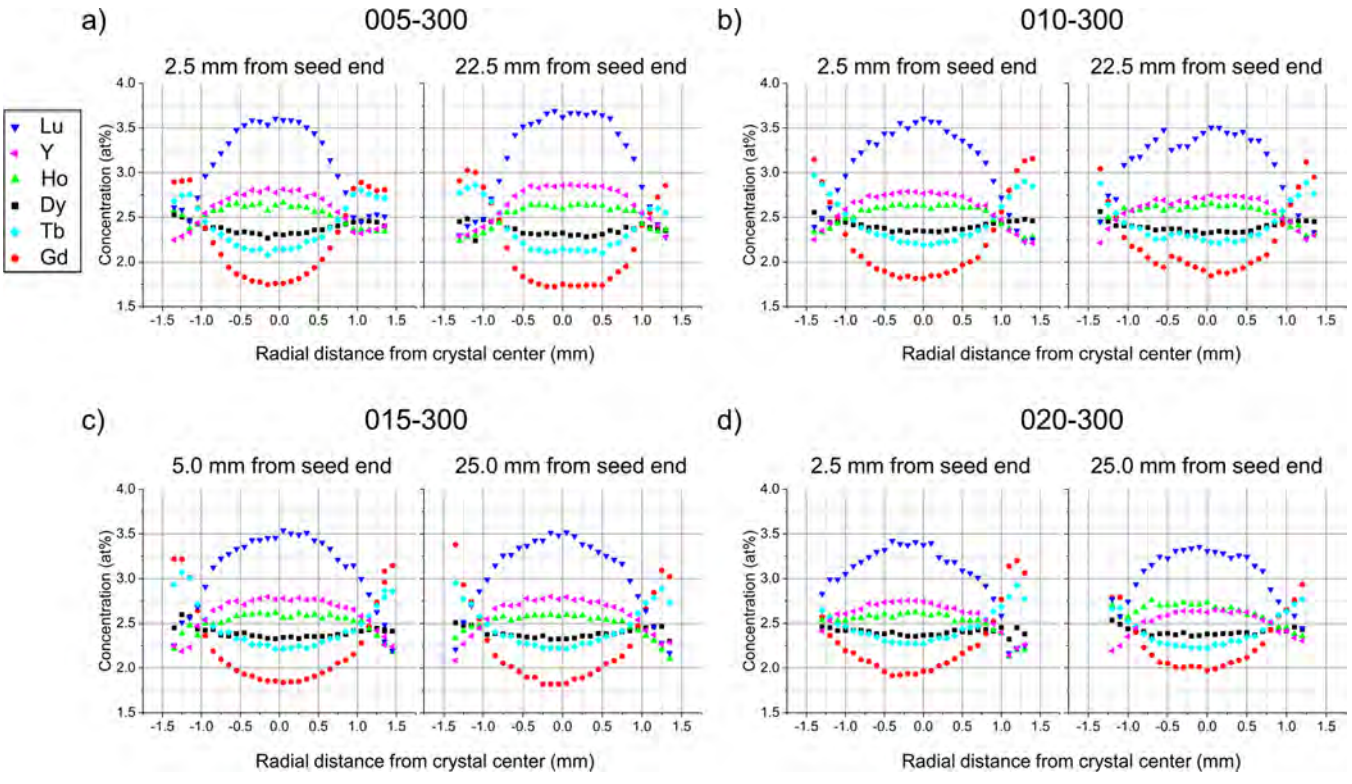

Figure 5. EPMA radial concentration profiles were measured at different ends of the crystals 005−300 (a), 010−300 (b), 015−300 (c), and 020−300 (d) that were grown with the same height of the molten zone but at different pulling rates. The legend by item (a) applies to all graphs. RE elemental profiles are closer to the nominal 2.5 atom % in crystals pulled at a faster rate. On the horizontal axis, zero represents the center of the crystal, while −1.5 or +1.5 mm represent the last measurement toward the outer surface of the crystal.

https://dx.doi.org/10.1021/acs.cgd.0c00887
Cryst. Growth Des. 2020, 20, 6769−6776

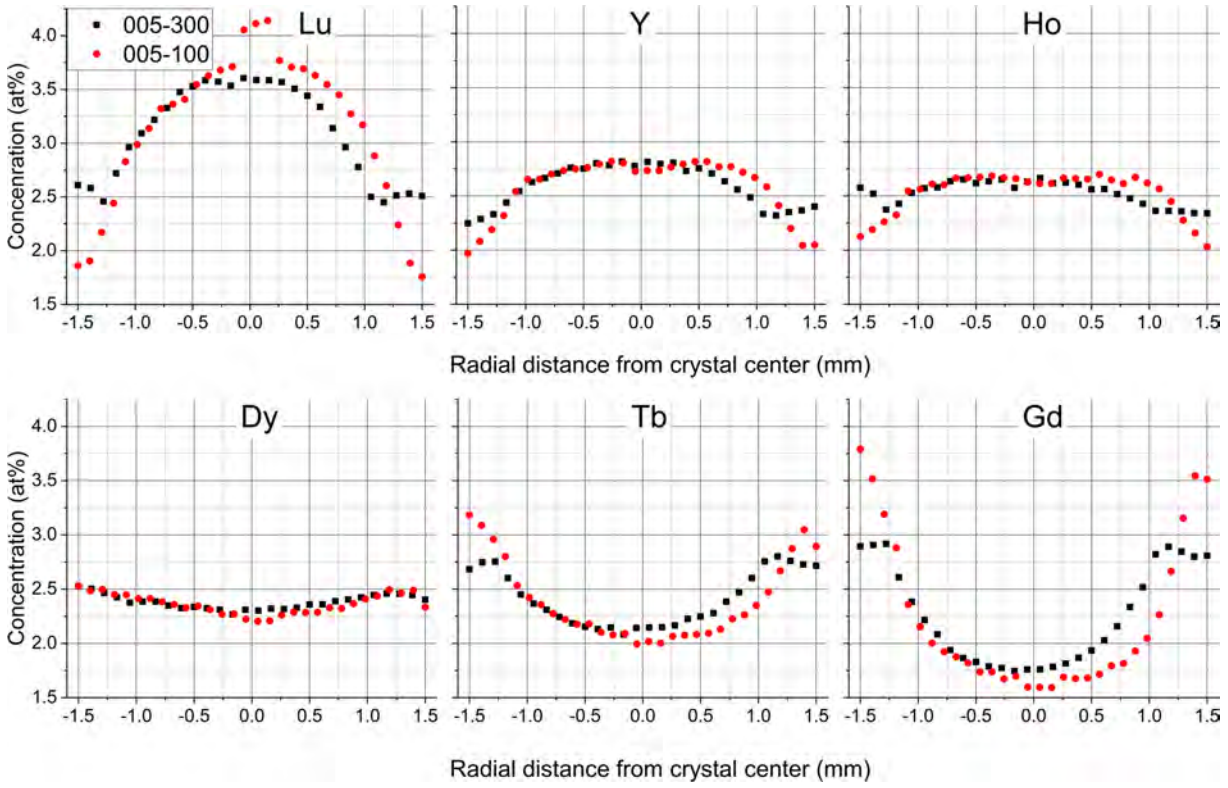

Figure 6. Comparison of EPMA radial concentration profiles for the crystals 005−300 (black ■) and 005−100 (red ●), both grown at 0.05 mm/min with a molten zone of 300 or 100 μm, respectively. Measurements were obtained at 2.5 mm from the seed end for both crystals. The RE stoichiometric concentration is 2.5 atom %.

consistent with the fact that ions smaller than the substituted element have a $k > 1$, while larger constituents have a $k < 1$.[43]

Our observations of the radial distribution of the REs in $(Lu_{1/6}Y_{1/6}Ho_{1/6}Dy_{1/6}Tb_{1/6}Gd_{1/6})_3Al_5O_{12}$ are consistent with previous reports on radial dopant distribution in micro-pulling-down crystals. Dopants that are smaller than the substituted host element usually concentrate in the center of the crystal, while larger dopants segregate toward the outer surface. This has been observed in fiber crystals of Cr- or Ga-doped Al_2O_3, Cr- or Tb-doped $Gd_3Ga_5O_{12}$, and Yb-doped $Y_3Al_5O_{12}$.[23] Dopant distribution profiles follow the same trend in the bulk crystals of Cr-, Nd-, Yb-, or Ce-doped $Y_3Al_5O_{12}$,[24] Nd-, Ho-, Er-, or Tm-doped $Lu_3Al_5O_{12}$,[25] and Pr-doped $YAlO_3$[44] and Y_2SiO_5.[45] Similarly, in $(Lu_{1/6}Y_{1/6}Ho_{1/6}Dy_{1/6}Tb_{1/6}Gd_{1/6})_3Al_5O_{12}$ RE that are smaller than the average ionic radius concentrate in the center of the crystal, while larger RE segregate toward the outer surface.

3.3.2. Effect of the Pulling Rate on Elemental Distribution. To investigate whether the pulling rate affects the radial elemental distribution, profiles were compared for crystals grown at different pulling rates in Figure 5. Two EPMA radial profiles are shown for each crystal. These were spaced widely apart along the growth axis, one close to the seed end and one close to the tail end. In the $RE_3Al_5O_{12}$ stoichiometry, the nominal atomic concentration of each RE element is 2.5 atom %. Faster pulling rates resulted in greater uniformity, promoting a flattening of the radial distribution profiles toward the nominal concentration. The radial profiles of the crystal pulled at 0.20 mm/min (020−300) are closer to 2.5 atom % than the profiles of the crystal pulled at 0.05 mm/min (005−300). With increasing pulling rates, there is a more intense melt flow from the crucible and a faster solidification rate, which limits the radial element diffusion and segregation. This explains the flattening of the distribution profiles in 020−300.

In general, REs with an ionic radius closer to the average RE radius in $(Lu_{1/6}Y_{1/6}Ho_{1/6}Dy_{1/6}Tb_{1/6}Gd_{1/6})_3Al_5O_{12}$ have profiles closer to 2.5 atom %, as shown in Figure 5. However, overall concentrations of Lu and Gd deviate significantly from the nominal value in all crystals; Lu is in excess, while Gd is deficient. A small amount of material did remain in the crucible capillary after growths were completed; if this remaining material is deficient in Lu and rich in Gd, it would explain the concentration deviation. It was not possible to verify the chemical composition of the remaining material, because it could not be removed from the crucible for analysis. A more likely explanation is that Lu concentrations might have been slightly overestimated due to extra counts from other RE in the EPMA measurements, specifically Dy, since their spectral lines overlap. Gadolinium, however, is the largest RE and would, therefore, have segregated farther toward the outer surface of the crystal outside the boundaries of the EPMA measurement. The deviation of the Lu and Gd concentrations is improved with the more intense melt flow and faster solidification rates that accompany faster pulling rates, consistent with limited diffusion and segregation.

Most of the individual elemental profiles in the eight plots in Figure 5 are radially symmetric with respect to the crystal vertical axis. One exception is the crystal 020−300, in which the profiles at 2.5 mm from the seed end are asymmetric. Similar asymmetry in dopant distribution profiles have been reported by others.[24,26] Although not shown in this manuscript, once a distance of 12.5 mm from the seed was achieved, the profiles of all REs in 020−300 became symmetric. Therefore, the initial asymmetry in RE radial distribution

https://dx.doi.org/10.1021/acs.cgd.0c00887
Cryst. Growth Des. 2020, 20, 6769−6776

may be attributed to a delay in reaching stable conditions due to stepwise increases in pulling rate required to achieve the target rate.

3.4. Axial Distribution. The axial elemental distribution was quite uniform as to be expected in many materials grown by the micro-pulling-down method.[35] We compare the two concentration profiles shown for each one of the four crystals: left versus right plots for each part of Figure 5a–d. One of the two profiles was measured at either 2.5 or 5.0 mm distant from the seed end, representing the portion of each crystal that crystallized first; the other profile was measured at either 22.5 or 25.0 mm distant from the seed end, representing the portion of the crystal that crystallized near the end of growth. Comparing the two plots in Figure 5a, clearly the overall content of the six REs did not vary significantly along the length of the crystals. The same general trend is observed for the other crystals in Figure 5b–d.

The EPMA radial profiles of the crystals 005–300 and 005–100, grown at the same pulling rate of 0.05 mm/min but with a different molten zone of 300 or 100 μm, respectively, are shown in Figure 6. There is no significant variation in the shape of the profile curves for all six cations. Closer to the outer edge of the crystals, the concentrations are closer to nominal in the crystal that was grown with a thicker molten zone, 005–300. This can be attributed to an enhanced mixing due to a more pronounced Marangoni flow close to the free surface of the melt, which is expected for thicker molten zones.[35,46]

4. CONCLUSION

For the first time we demonstrated successful crystal growth of the complex high-entropy aluminum garnet $(Lu_{1/6}Y_{1/6}Ho_{1/6}Dy_{1/6}Tb_{1/6}Gd_{1/6})_3Al_5O_{12}$ using the micro-pulling-down method. These crystals are readily grown with excellent reproducibility in terms of molten zone height, diameter control, surface transparency, and optical quality. All crystals grown had a single-phase garnet structure with a space group $Ia\bar{3}d$ and a relatively homogeneous axial composition. We established that radial distribution of elements in the crystals is associated with their ionic radii. Smaller REs concentrate in the center of the crystal, while larger elements segregate toward the outer surface. Faster pulling rates were found to have a favorable effect on flattening the radial nonuniformity.

Further investigation into high-entropy aluminum garnets may reveal attractive functional properties in this and similar systems, as previously demonstrated in other high-entropy oxides. This may be of particular value for applications that require crystals with high optical quality, such as lasing and scintillation. The crystalline environment strongly affects structural and functional properties; therefore, a homogeneous elemental distribution is required to design a material with a desired performance. Understanding of the mechanism for incorporation of principal elements in a multicomponent crystal lattice leads to selection of the most suitable crystal growth technique for larger-size crystals for commercial applications.

■ ASSOCIATED CONTENT

Supporting Information

The Supporting Information is available free of charge at https://pubs.acs.org/doi/10.1021/acs.cgd.0c00887.

Figure comparing molten zone heights, tables for singe-crystal X-ray diffraction refinement data, EPMA radial elemental profiles along the 005–300 crystal (PDF)

Accession Codes

CCDC 2014693–2014694 contain the supplementary crystallographic data for this paper. These data can be obtained free of charge via www.ccdc.cam.ac.uk/data_request/cif, or by emailing data_request@ccdc.cam.ac.uk, or by contacting The Cambridge Crystallographic Data Centre, 12 Union Road, Cambridge CB2 1EZ, UK; fax: +44 1223 336033.

■ AUTHOR INFORMATION

Corresponding Author

Matheus Pianassola − *Scintillation Materials Research Center and Department of Materials Science and Engineering, University of Tennessee, Knoxville, Tennessee 37996, United States;* orcid.org/0000-0001-7468-2794; Email: mpianass@vols.utk.edu

Authors

Madeline Loveday − *Scintillation Materials Research Center and Department of Materials Science and Engineering, University of Tennessee, Knoxville, Tennessee 37996, United States*

Bryan C. Chakoumakos − *Neutron Scattering Division, Oak Ridge National Laboratory, Oak Ridge, Tennessee 37831, United States*

Merry Koschan − *Scintillation Materials Research Center, University of Tennessee, Knoxville, Tennessee 37996, United States*

Charles L. Melcher − *Scintillation Materials Research Center, Department of Materials Science and Engineering, and Department of Nuclear Engineering, University of Tennessee, Knoxville, Tennessee 37996, United States*

Mariya Zhuravleva − *Scintillation Materials Research Center and Department of Materials Science and Engineering, University of Tennessee, Knoxville, Tennessee 37996, United States*

Complete contact information is available at: https://pubs.acs.org/10.1021/acs.cgd.0c00887

Notes

The authors declare no competing financial interest.

■ ACKNOWLEDGMENTS

This project was supported by the National Science Foundation (DMR 1846935). One of the authors is grateful for the support from the Center for Materials Processing, University of Tennessee. Electron microprobe measurements were performed at the Electron Microprobe Laboratory in the Department of Earth and Planetary Sciences at the University of Tennessee, Knoxville, with the assistance of M. McCanta and A. Patchen. X-ray diffraction experiments were performed at the Joint Institute for Advanced Materials Diffraction Facility located at the University of Tennessee, Knoxville. A portion of this research used resources at the Spallation Neutron Source, a Department of Energy Office of Science User Facility operated by the Oak Ridge National Laboratory.

■ REFERENCES

(1) Musicó, B. L.; Gilbert, D.; Ward, T. Z.; Page, K.; George, E.; Yan, J.; Mandrus, D.; Keppens, V. The emergent field of high entropy

oxides: Design, prospects, challenges, and opportunities for tailoring material properties. *APL Mater.* **2020**, *8*, 040912.
(2) Ikesue, A.; Aung, Y. L.; Taira, T.; Kamimura, T.; Yoshida, K.; Messing, G. L. Progress in ceramic lasers. *Annu. Rev. Mater. Res.* **2006**, *36*, 397−429.
(3) Nikl, M.; Yoshikawa, A.; Kamada, K.; Nejezchleb, K.; Stanek, C. R.; Mares, J. A.; Blazek, K. Development of LuAG-based scintillator crystals - A review. *Prog. Cryst. Growth Charact. Mater.* **2013**, *59*, 47−72.
(4) Li, J. G.; Sakka, Y. Recent progress in advanced optical materials based on gadolinium aluminate garnet ($Gd_3Al_5O_{12}$). *Sci. Technol. Adv. Mater.* **2015**, *16*, 014902.
(5) Kamada, K.; Yanagida, T.; Pejchal, J.; Nikl, M.; Endo, T.; Tsutumi, K.; Fujimoto, Y.; Fukabori, A.; Yoshikawa, A. Scintillator-oriented combinatorial search in Ce-doped $(Y,Gd)_{(3)}(Ga,Al)_{(5)}O$-12 multicomponent garnet compounds. *J. Phys. D: Appl. Phys.* **2011**, *44*, 505104.
(6) Kamada, K.; Endo, T.; Tsutumi, K.; Yanagida, T.; Fujimoto, Y.; Fukabori, A.; Yoshikawa, A.; Pejchal, J.; Nikl, M. Composition Engineering in Cerium-Doped $(Lu,Gd)_{(3)}(Ga,Al)_{(5)}O$-12 Single-Crystal Scintillators. *Cryst. Growth Des.* **2011**, *11*, 4484−4490.
(7) Prusa, P.; Kamada, K.; Nikl, M.; Yoshikawa, A.; Mares, J. A. Light yield of $(Lu, Y, Gd)_{(3)}Al_2Ga_3O_{12}$:Ce garnets. *Radiat. Meas.* **2013**, *56*, 62−65.
(8) Chewpraditkul, W.; Panek, D.; Bruza, P.; Chewpraditkul, W.; Wanarak, C.; Pattanaboonmee, N.; Babin, V.; Bartosiewicz, K.; Kamada, K.; Yoshikawa, A.; Nikl, M. Luminescence properties and scintillation response in Ce^{3+}-doped $Y_2Gd_1Al_{5-x}Ga_xO_{12}$ (x = 2, 3, 4) single crystals. *J. Appl. Phys.* **2014**, *116*, 083505.
(9) Zorenko, Y.; Gorbenko, V.; Savchyn, V.; Zorenko, T.; Fedorov, A.; Sidletskiy, O. Development of scintillating screens based on the single crystalline films of Ce doped $(Gd,Y)(3)(Al,Ga,Sc)(5)O$-12 multi-component garnets. *J. Cryst. Growth* **2014**, *401*, 532−536.
(10) Chewpraditkul, W.; Bruza, P.; Panek, D.; Pattanaboonmee, N.; Wantong, K.; Chewpraditkul, W.; Babin, V.; Bartosiewicz, K.; Kamada, K.; Yoshikawa, A.; Nikl, M. Optical and scintillation properties of Ce3+-doped $YGd_2Al_{5-x}Ga_xO_{12}$ (x = 2,3,4) single crystal scintillators. *J. Lumin.* **2016**, *169*, 43−50.
(11) Miracle, D. B.; Senkov, O. N. A critical review of high entropy alloys and related concepts. *Acta Mater.* **2017**, *122*, 448−511.
(12) Rost, C. M.; Sachet, E.; Borman, T.; Moballegh, A.; Dickey, E. C.; Hou, D.; Jones, J. L.; Curtarolo, S.; Maria, J. P. Entropy-stabilized oxides. *Nat. Commun.* **2015**, *6*. DOI: 10.1038/ncomms9485
(13) Djenadic, R.; Sarkar, A.; Clemens, O.; Loho, C.; Botros, M.; Chakravadhanula, V. S. K.; Kübel, C.; Bhattacharya, S. S.; Gandhi, A. S.; Hahn, H. Multicomponent equiatomic rare earth oxides. *Mater. Res. Lett.* **2017**, *5*, 102−109.
(14) Pianassola, M.; Loveday, M.; McMurray, J. W.; Koschan, M.; Melcher, C. L.; Zhuravleva, M. Solid-state synthesis of multi-component equiatomic rare-earth oxides. *J. Am. Ceram. Soc.* **2020**, *103*, 2908−2918.
(15) Ren, X.; Tian, Z.; Zhang, J.; Wang, J. Equiatomic quaternary $(Y_{1/4}Ho_{1/4}Er_{1/4}Yb_{1/4})_2SiO_5$ silicate: A perspective multifunctional thermal and environmental barrier coating material. *Scr. Mater.* **2019**, *168*, 47−50.
(16) Chen, H.; Xiang, H.; Dai, F.-Z.; Liu, J.; Zhou, Y. High entropy (Yb0.25Y0.25Lu0.25Er0.25)2SiO5 with strong anisotropy in thermal expansion. *J. Mater. Sci. Technol.* **2020**, *36*, 134−139.
(17) Zhao, Z.; Xiang, H.; Dai, F.-Z.; Peng, Z.; Zhou, Y. $(La_{0.2}Ce_{0.2}Nd_{0.2}Sm_{0.2}Eu_{0.2})_2Zr_2O_7$: A novel high-entropy ceramic with low thermal conductivity and sluggish grain growth rate. *J. Mater. Sci. Technol.* **2019**, *35*, 2647−2651.
(18) Zhao, Z.; Chen, H.; Xiang, H.; Dai, F.-Z.; Wang, X.; Peng, Z.; Zhou, Y. $(La_{0.2}Ce_{0.2}Nd_{0.2}Sm_{0.2}Eu_{0.2})PO_4$: A high-entropy rare-earth phosphate monazite ceramic with low thermal conductivity and good compatibility with Al_2O_3. *J. Mater. Sci. Technol.* **2019**, *35*, 2892−2896.
(19) Zhao, Z.; Chen, H.; Xiang, H.; Dai, F.-Z.; Wang, X.; Xu, W.; Sun, K.; Peng, Z.; Zhou, Y. High-entropy $(Y_{0.2}Nd_{0.2}Sm_{0.2}Eu_{0.2}Er_{0.2})$-$AlO_3$: A promising thermal/environmental barrier material for oxide/oxide composites. *J. Mater. Sci. Technol.* **2020**, *47*, 45−51.
(20) Chen, H.; Zhao, Z.; Xiang, H.; Dai, F.-Z.; Xu, W.; Sun, K.; Liu, J.; Zhou, Y. High entropy $(Y_{0.2}Yb_{0.2}Lu_{0.2}Eu_{0.2}Er_{0.2})$3Al5O12: A novel high temperature stable thermal barrier material. *J. Mater. Sci. Technol.* **2020**, *48*, 57−62.
(21) Sharma, Y.; Musico, B. L.; Gao, X.; Hua, C.; May, A. F.; Herklotz, A.; Rastogi, A.; Mandrus, D.; Yan, J.; Lee, H. N.; Chisholm, M. F.; Keppens, V.; Ward, T. Z. Single-crystal high entropy perovskite oxide epitaxial films. *Physical Review Materials* **2018**, *2*. DOI: 10.1103/PhysRevMaterials.2.060404
(22) Shannon, R. D.; Prewitt, C. T. Effective Ionic Radii in Oxides and Fluorides. *Acta Crystallogr., Sect. B: Struct. Crystallogr. Cryst. Chem.* **1969**, *25*, 925−946.
(23) Maier, D.; Rhede, D.; Bertram, R.; Klimm, D.; Fornari, R. Dopant segregations in oxide single-crystal fibers grown by the micro-pulling-down method. *Opt. Mater.* **2007**, *30*, 11−14.
(24) Simura, R.; Yoshikawa, A.; Uda, S. The radial distribution of dopant (Cr, Nd, Yb, or Ce) in yttrium aluminum garnet ($Y_3Al_5O_{12}$) single crystals grown by the micro-pulling-down method. *J. Cryst. Growth* **2009**, *311*, 4763−4769.
(25) Sugiyama, M.; Yokota, Y.; Fujimoto, Y.; Yanagida, T.; Futami, Y.; Kurosawa, S.; Yoshikawa, A. Dopant segregation in rare earth doped lutetium aluminum garnet single crystals grown by the micro-pulling down method. *J. Cryst. Growth* **2012**, *352*, 110−114.
(26) Yokota, Y.; Kudo, T.; Chani, V.; Ohashi, Y.; Kurosawa, S.; Kamada, K.; Zeng, Z.; Kawazoe, Y.; Yoshikawa, A. Improvement of dopant distribution in radial direction of single crystals grown by micro-pulling-down method. *J. Cryst. Growth* **2017**, *474*, 178−182.
(27) Uda, S.; Kon, J.; Shimamura, K.; Fukuda, T. Analysis of Ge distribution in $Si_{1-x}Ge_x$ single crystal fibers by the micro-pulling down method. *J. Cryst. Growth* **1996**, *167*, 64−73.
(28) Cockayne, B.; Gasson, D. B.; Findlay, D.; Goodwin, D. W.; Clay, R. A. The growth and laser characteristics of yttrium-gadolinium-aluminium garnet single crystals. *J. Phys. Chem. Solids* **1968**, *29*, 905−910.
(29) Ivanov, A. O.; Mochalov, I. V.; Tkachuk, A. M.; Fedorov, V. A.; Feofilov, P. P. Emission of $\lambda \approx 2\ \mu$ stimulated radiation by holmium in aluminum holmium garnet crystals. *Soviet Journal of Quantum Electronics* **1975**, *5*, 186−188.
(30) Miyazawa, Y.; Mori, M.; Honma, S. Interface Shape Transitions in Czochralski Growth of $Dy_3Al_5O_{12}$. *J. Cryst. Growth* **1978**, *43*, 541−542.
(31) Wu, P.; Pelton, A. D. Coupled Thermodynamic Phase-Diagram Assessment of the Rare-Earth-Oxide Aluminum-Oxide Binary-Systems. *J. Alloys Compd.* **1992**, *179*, 259−287.
(32) Ganschow, S.; Klimm, D.; Reiche, P.; Uecker, R. On the crystallization of terbium aluminium garnet. *Cryst. Res. Technol.* **1999**, *34*, 615−619.
(33) Ganschow, S.; Klimm, D.; Epelbaum, B. M.; Yoshikawa, A.; Doerschel, J.; Fukuda, T. Growth conditions and composition of terbium aluminum garnet single crystals grown by the micro pulling down technique. *J. Cryst. Growth* **2001**, *225*, 454−457.
(34) Geho, M.; Sekijima, T.; Fujii, T. Growth mechanism of incongruently melting terbium aluminum garnet ($Tb_3Al_5O_{12}$; TAG) single crystals by laser FZ method. *J. Cryst. Growth* **2005**, *275*, e663−e667.
(35) Fukuda, T.; Chani, V. I. *Shaped Crystals: Growth by Micro-Pulling-Down Technique;* Springer: Berlin, Germany, 2007; Vol. *8*.
(36) Rigaku. *CrystalClear;* Rigaku Corporation: Tokyo, Japan, 2005.
(37) Sheldrick, G. M. A short history of SHELX. *Acta Crystallogr., Sect. A: Found. Crystallogr.* **2008**, *A64*, 112−122.
(38) Farrugia, L. J. WinGX and ORTEP for Windows: an update. *J. Appl. Crystallogr.* **2012**, *45*, 849−854.
(39) Emiraliev, A.; K, A. G.; Bakradze, R. V.; Karimov, U.; Ahmetzhanov, Z. I. The neutron diffraction redefinition of the coordinates of the atoms of oxygen in yttrio-aluminium garnet. *Kristallografiya* **1976**, *21*, 211−213.

https://dx.doi.org/10.1021/acs.cgd.0c00887
Cryst. Growth Des. 2020, 20, 6769−6776

(40) Euler, F.; Bruce, J. A. Oxygen Coordinates of Compounds with Garnet Structure. *Acta Crystallogr.* **1965**, *19*, 971−978.
(41) Kimura, H.; Sakamoto, M.; Numazawa, T.; Sato, M.; Maeda, H. Crystal-Growth of Large Size $Dy_3Al_5O_{12}$ Garnet Single-Crystals. *J. Cryst. Growth* **1990**, *99*, 850−853.
(42) Slack, G. A.; Oliver, D. W. Thermal Conductivity of Garnets and Phonon Scattering by Rare-Earth Ions. *Phys. Rev. B* **1971**, *4*, 592−609.
(43) Brandle, C. D.; Valentino, A. J.; Berkstresser, G. W. Czochralski Growth Of Rare-Earth Orthosilicates (Ln_2SiO_5). *J. Cryst. Growth* **1986**, *79*, 308−315.
(44) Zhuravleva, M.; Novoselov, A.; Yoshikawa, A.; Pejchal, J.; Nikl, M.; Fukuda, T. Scintillating Properties of Pr-Doped $YAlO_3$ Single Crystals Grown by the Micro-pulling-Down Method. *Inorg. Mater.* **2007**, *43*, 753−757.
(45) Novoselov, A.; Ogino, H.; Yoshikawa, A.; Nikl, M.; Pejchal, J.; Beitlerova, A.; Fukuda, T. Crystal growth, optical and luminescence properties of Pr-doped Y_2SiO_5 single crystals. *Opt. Mater.* **2007**, *29*, 1381−1384.
(46) Samanta, G.; Yeckel, A.; Daggolu, P.; Fang, H.; Bourret-Courchesne, E. D.; Derby, J. J. Analysis of limits for sapphire growth in a micro-pulling-down system. *J. Cryst. Growth* **2011**, *335*, 148−159.

https://dx.doi.org/10.1021/acs.cgd.0c00887
Cryst. Growth Des. 2020, 20, 6769−6776